

Evidence for anoxic shallow oceans at 2.45 Ga: Implications for the rise of oxygenic photosynthesis

Birger Rasmussen^{1*}, Janet R. Muhling¹, Nicholas J. Tosca², and Harilaos Tsikos³

¹School of Earth Sciences, The University of Western Australia, Perth, Western Australia 6009, Australia

²Department of Earth Sciences, University of Oxford, South Parks Road, Oxford OX1 3AN, UK

³Geology Department, Rhodes University, Artillery Road, Grahamstown 6140, South Africa

ABSTRACT

Geochemical proxies indicate that atmospheric oxygen levels were $<10^{-5}$ times present atmospheric levels ($10^{-5} \times \text{PAL}$) until the start of the Great Oxidation Event (GOE; 2.33 Ga). However, trace metal and isotopic data from sedimentary rocks have been interpreted to reflect the presence of oxygenated surface oceans ≥ 2.5 b.y. ago, implying decoupling of the atmosphere and shallow marine systems. Evidence for oxygen in shallow oceans has fueled the idea that oxygenic photosynthesis evolved long before the GOE and that oxygen did not accumulate in the atmosphere because it was scavenged by reductants such as dissolved Fe^{2+} , a process thought by some to have formed banded iron formations (BIFs). Here we present high-resolution microscopy showing that 2.45 Ga shallow-water BIFs were deposited as ferrous iron-rich muds dominantly composed of greenalite; these muds were rapidly cemented by silica on the seafloor, and subsequently eroded and redeposited as intraformational chert clasts. Our experimental results and kinetic models show that the accumulation of greenalite required seawater oxygen concentrations $<10^{-6} \times \text{PAL}$ on the shallow shelf. We infer that oxygen levels of the surface oceans and atmosphere were not decoupled 2.45 b.y. ago, but that both were exceedingly low ($<10^{-5} \times \text{PAL}$). Our findings support the hypothesis that oxygenic photosynthesis evolved shortly before atmospheric oxygenation and was a direct cause of the GOE.

INTRODUCTION

After an anoxic beginning, Earth's surface experienced a major rise in atmospheric oxygen, the Great Oxidation Event (GOE). The age of the GOE, marked by the disappearance of mass-independent fractionation of multiple S isotopes (MIF-S) in sedimentary sulfides, is estimated to be ca. 2.33 Ga (Luo et al., 2016) and interpreted to signify a rise in baseline oxygen concentrations above 10^{-5} times present atmospheric levels ($10^{-5} \times \text{PAL}$) (Pavlov and Kasting, 2002; Luo et al., 2016). It is generally agreed that free oxygen in the oceans and atmosphere resulted from the evolution of oxygenic photosynthesis in Cyanobacteria (Fischer et al., 2016), however the timing of this event has been difficult to constrain. The oldest unambiguous cyanobacterial microfossils (ca. 1.9 Ga) post-date the GOE, while estimates based on molecular clocks depend on the selection of calibration points (Fischer et al., 2016; Shih et al., 2017).

The uncertainty has resulted in two schools of thought. The first favors the evolution of oxygenic Cyanobacteria hundreds of millions of years before the GOE, with oxygen consumed by redox buffers such as CH_4 and Fe^{2+} in the oceans, preventing its accumulation in the atmosphere (Zahnle et al., 2006; Kump and Barley, 2007; Czaja et al., 2012; Satkoski et al., 2015). The second posits that oxygenic photosynthesis evolved just prior to the GOE, with rapid elimination of oxygen sinks and atmospheric accumulation (Fischer et al., 2016; Ward et al., 2016).

An accurate understanding of the redox chemistry of the Archean ocean can be gleaned from banded iron formations (BIFs), which are chemical sedimentary rocks comprising alternating layers of iron-rich and silica-rich minerals. They have been widely used to interpret oxygen levels in the pre-GOE oceans, however aspects of their origin are controversial. The traditional view is that BIFs were deposited as ferric oxides and/or hydroxides that formed in

the water column by biologically driven oxidation (Beukes and Gutzmer, 2008; Fischer and Knoll, 2009; Konhauser et al., 2017). Following deposition, the ferric oxides and/or hydroxides were converted to iron-rich minerals, including hematite, magnetite, siderite, and stilpnomelane.

In contrast, recent studies suggest that iron was deposited abiotically as nanometer-sized particles of greenalite [$(\text{Fe})_3\text{Si}_2\text{O}_5(\text{OH})_4$] in anoxic seawater (Rasmussen et al., 2015a, 2015b, 2017; Johnson et al., 2018). The microfabric of the greenalite nanoparticles preserved in early diagenetic chert cement, which resembles freshly deposited muds (Rasmussen et al., 2019), supports a depositional origin (Rasmussen et al., 2015a, 2015b, 2017, 2019; Johnson et al., 2018). According to this model, most of the greenalite was replaced after deposition by iron oxides, iron carbonates, and iron silicates, except in intervals of well-preserved laminated chert.

To date, greenalite nanoparticles have been identified only in deeper-water BIFs and cherts, leading to the suggestion that it was restricted to anoxic deep-water environments, while on the shallow shelf, $\text{Fe}^{2+}(\text{aq})$ was rapidly converted to ferric oxide and/or hydroxide by photosynthesis-related oxidation pathways (Konhauser et al., 2017). Establishing the primary mineralogy of the chemical sediments in shallow-water environments is crucial in deciphering the origin of BIFs, and hence unravelling what they tell us about the redox chemistry of the oceans and atmosphere, and biological processes on early Earth. Here we investigate iron formations deposited within the photic zone of an extensive shallow-water shelf ~2.45 b.y. ago.

GEOLOGICAL SETTING AND SAMPLES

The Griquatown Iron Formation in Griqualand West, South Africa (Fig. 1), was deposited between 2.46 Ga and 2.42 Ga (Beukes

*E-mail: birger.rasmussen@uwa.edu.au

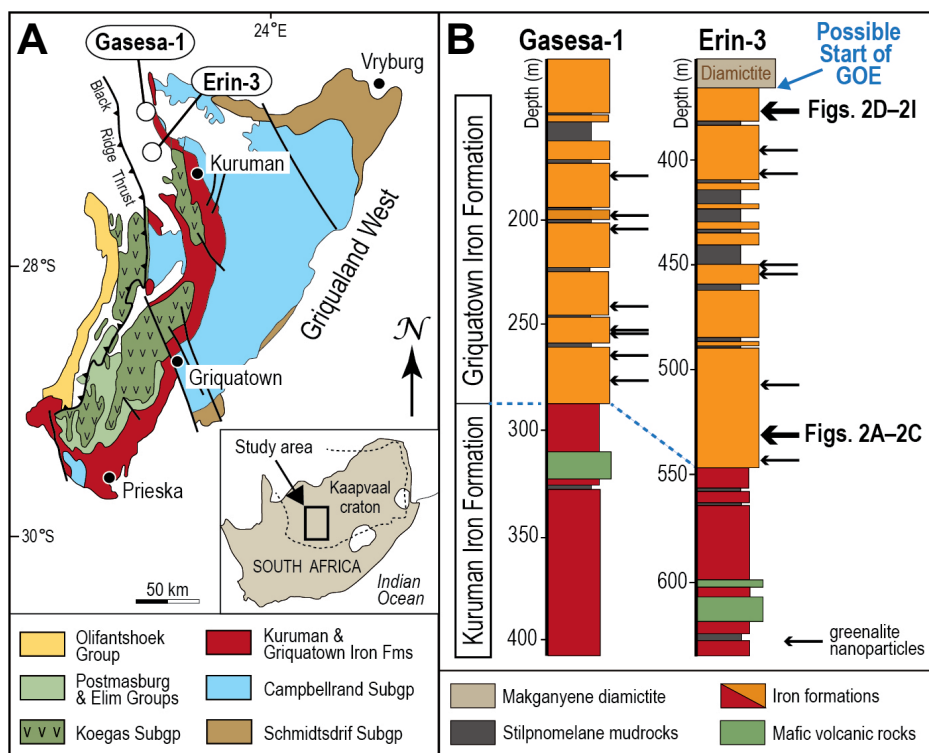


Figure 1. Location map and stratigraphic column. A: Regional geology map of Griqualand West Basin, Kaapvaal craton, South Africa, showing location of drill holes (Gasesa-1 and Erin-3, drilled by Samancor Chrome [Sandton, South Africa]) containing samples studied here. B: Stratigraphic column showing simplified lithology, stratigraphic units, and sample location (black arrows) in drill-holes Gasesa-1 and Erin-3. GOE—Great Oxidation Event; Fm—Formation; Subgp—Subgroup.

and Gutzmer, 2008). It overlies the Kuruman Iron Formation and underlies the Makganyene diamictite, which has been linked to the start of the GOE. We collected diamond drill-core samples from two drill holes drilled by Samancor Chrome (Sandton, South Africa) in the early 1990s (Gasesa-1 and Erin-3), which intersect the Griquatown Iron Formation and overlie Makganyene diamictite (Fig. 1). The Griquatown Iron Formation is the best-preserved shallow-water iron formation that predates the GOE. It is ~250 m thick with consistent lithofacies over a strike length of ~500 km (Beukes, 1984). It comprises beds of thinly laminated sideritic and greenalitic BIF intercalated with thick beds of intraclastic chert and carbonate (Beukes, 1984; Beukes and Gutzmer, 2008). The chert and carbonate intraclasts have been linked to the erosion and redeposition of silicified sideritic hardgrounds by wave action (Beukes, 1984). The presence of cross lamination and ooids in the intraclastic iron formation indicate that deposition occurred in a shallow-water environment above wave base, in water depths between 50 and 100 m to possibly <10 m near the top of the succession (Beukes, 1984; Beukes and Gutzmer, 2008). Although the dominant iron minerals are now siderite and greenalite, iron oxides are inferred to have been the primary iron precipitate, with greenalite,

siderite, and magnetite resulting from diagenetic dissimilatory iron reduction (Beukes and Gutzmer, 2008).

We carried out optical and scanning electron microscopy (SEM) on polished thin sections of the iron formation samples, allowing us to document textural relationships between early-formed phases and to identify suitable areas for transmission electron microscopy (TEM). From these, thin foils were cut by focused ion beam (FIB) and examined by high-resolution TEM.

RESULTS AND DISCUSSION

Petrography of Greenalite-Rich Intraclastic Chert Beds

Beds of intraclastic chert collected from both drill holes vary in thickness from several centimeters to tens of centimeters, and comprise sand- to pebble-sized chert clasts (Fig. 2). Chert intraclasts are subrounded to well rounded, and beds are poorly sorted with a mud-sized matrix engulfed in chert cement (Fig. 2). The clasts do not show internal lamination, although adjacent clasts are discernible due to subtle variations in color.

Chert grains and interstitial cement contain abundant nanometer-sized plates of greenalite (Fig. 2). TEM—energy dispersive X-ray spectroscopy (EDS) maps show that the particles

are composed of Fe, Si, and O, with minor Al and Mg (Fig. DR1 in the GSA Data Repository¹), while diffraction data confirm the (001) d-spacing (0.72 nm) and modulation (2.2 nm) characteristic of greenalite (Guggenheim et al., 1982; Tosca et al., 2016).

Individual plates are randomly oriented and vary in size from 10 to 500 nm in width and 1 to 50 nm in thickness. Their random orientation and uniform distribution are identical to the fabric of greenalite in deeper-water BIFs (Rasmussen et al., 2015a, 2017). This fabric closely resembles the texture of clay slurries (Deirich et al., 2018) and modern marine muds (Bennett et al., 1981; Kase et al., 2016), supporting a depositional origin for the greenalite particles (Rasmussen et al., 2019). The preservation of depositional textures in parts of the chert implies that early diagenetic silica cementation “froze” the original fabric of the chemical muds, minimizing the effects of diagenesis, burial-related compaction, and metamorphism.

The presence of greenalite nanoparticles in intraclastic chert grains (Fig. 2) indicates that the original sediment was probably an iron-silicate mud deposited from the photic zone of the overlying water column and accumulated on the seafloor. After deposition, silica precipitated as a pore-filling cement (comprising 70–90%) that occluded primary porosity. The silicified muds were subjected to episodic high-energy wave action that scoured the seafloor and redeposited abraded clasts as chert and carbonate sandstones and conglomerates (cf. Beukes and Gutzmer, 2008). The presence of greenalite nanoparticles in matrix between chert clasts suggests that iron-silicate muds settled out of suspension prior to a second phase of seafloor silica cementation.

Greenalite nanoparticles occur throughout the iron formation (Fig. 1), but in most places they have been destroyed and replaced by secondary phases such as minnesotaite, riebeckite, siderite, ankerite, magnetite, hematite, and chert, as documented in deeper-water BIFs (Rasmussen et al., 2015a, 2017). Although hematite may now be more abundant than greenalite, petrographic and paleomagnetic studies suggest that much of the oxide formed long after deposition. Therefore, greenalite was likely much more abundant than hematite prior to post-depositional alteration and recrystallization.

The greenalite nanoparticles described here are identical to those preserved in the deeper-water BIFs and cherts of the Campbellrand Subgroup of South Africa (Rasmussen et al., 2017) and those of the Hamersley Group of Western Australia (Rasmussen et al., 2015a, 2015b). These observations suggest that greenalite was

¹GSA Data Repository item 2019122, methods, calculation of seawater O₂, and Figures DR1–DR7, is available online at <http://www.geosociety.org/datarepository/2019/>, or on request from editing@geosociety.org.

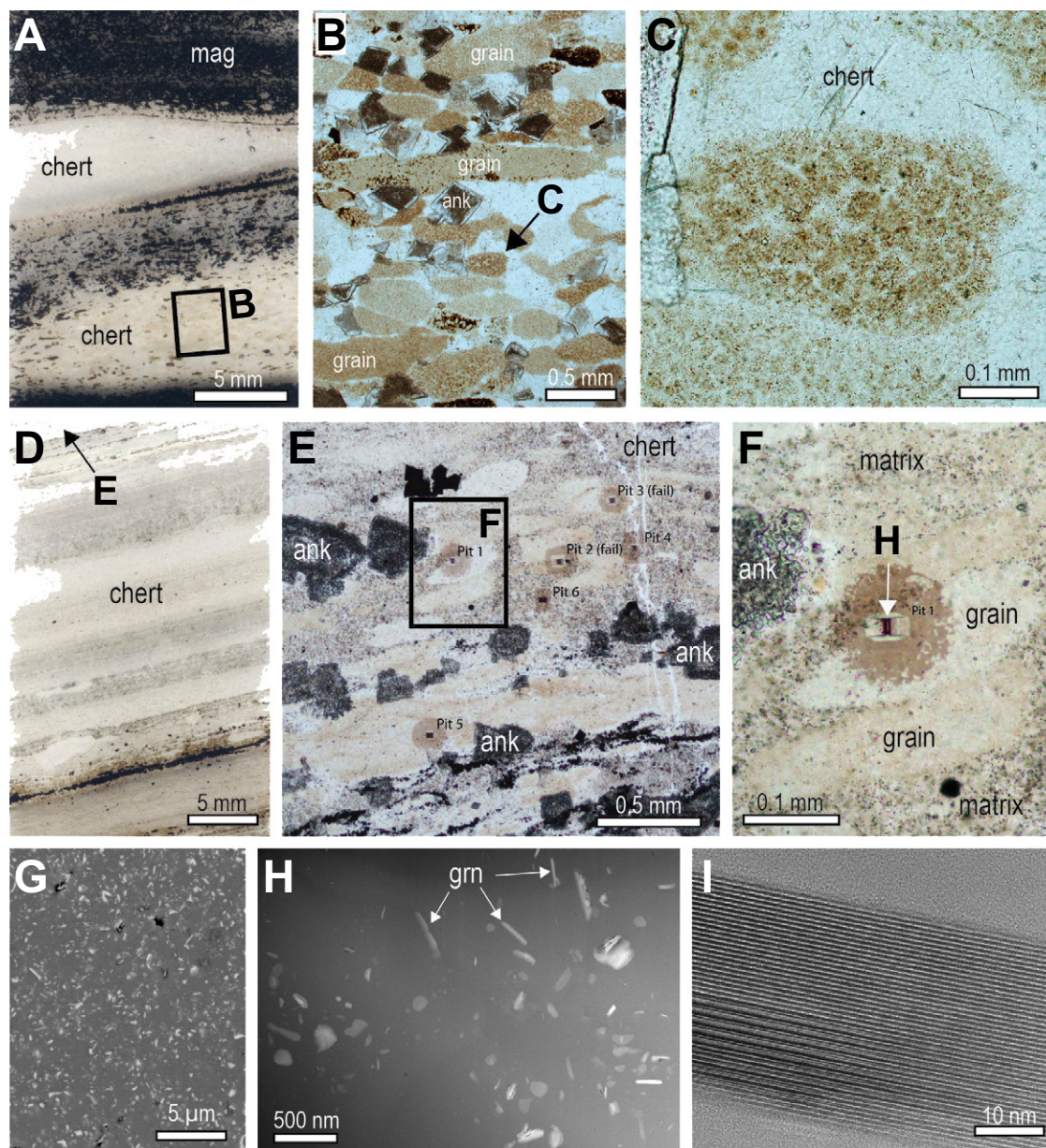


Figure 2. A: Plane polarized light (PPL) image of thin section of chert (mag—magnetite). B: PPL image of chert showing elongate clasts of greenalite-bearing chert and ankerite (ank). C: PPL close-up of chert grain with abundant greenalite nanoparticles and polygonal texture. D: PPL image of thin section of laminated chert. E: PPL image of chert with elongate clasts of greenalite-bearing chert and ankerite (ank). F: PPL image of elongate chert grain (see inset in E) showing pit where transmission electron microscopy (TEM) foil was removed by focused ion beam. G: Back-scattered electron (BSE) image of chert with abundant minute greenalite particles (light gray). H: High-angle annular dark field (HAADF) STEM image of foil cut from chert showing abundant, randomly oriented plates of iron silicate (light gray) in chert cement (gray) (grn—greenalite). I: High-resolution TEM image of greenalite particle. A–C are from drill-hole Erin-3, 530.0 m depth; D–I are from drill-hole Erin-3, 376.3 m depth (see Fig. 1B).

deposited not only on the basin floor and slope (Rasmussen et al., 2015a, 2017), but also in the photic zone of shallow shelf environments.

Kinetic Modeling of Greenalite Precipitation

To constrain dissolved $O_2(aq)$ concentrations under which the precipitation rate of greenalite would have outpaced the oxidation rate of Fe(II) in the Griquatown water column, we developed a kinetic model that accurately represents available experimental measurements of both processes. First, using time-resolved Fe(II) and $SiO_2(aq)$ concentrations from anoxic Fe(II)-silicate nucleation experiments conducted by Tosca et al. (2016), we constrained the total precipitation rate as a function of greenalite supersaturation (which is controlled by pH, $[Fe^{2+}]$, and $[SiO_2(aq)]$). Because it is characterized by low surface energy and high solubility,

the freshly precipitated structural precursor to greenalite is composed of many small particles (several tens to hundreds of nanometers), rather than fewer large crystals. The overall precipitation rate is dominated by nucleation phenomena rather than crystal growth (Tosca et al., 2016); thus, these experimental data are well described by classical nucleation rate theory (Lasaga, 1998). Because nucleation rate carries a strong exponential dependence on supersaturation (Lasaga, 1998), greenalite precipitation rates are prohibitively slow at values less than the “critical supersaturation” identified by Tosca et al. (2016) (Fig. DR2).

Dissolved Fe(II) may be oxidized by microbial processes or by dissolved $O_2(aq)$. Because the rates of microbial Fe(II) oxidation are typically much faster than abiotic oxidation by $O_2(aq)$ (Konhauser et al., 2007), our consideration of only the latter process yields conser-

vative maximum estimates of seawater $O_2(aq)$ concentrations. In order to calculate abiotic Fe(II) oxidation rates in Archean seawater, the effects of pH, Fe(II) concentration, and pCO_2 must be taken into account. For example, although the Fe(II)-oxidation rate in modern seawater is well constrained, experimental measurements in carbonated seawater show that the elevated dissolved CO_2 concentrations expected for shallow Archean seawater are likely to have enhanced Fe(II) oxidation rates (Millero et al., 1987). To take this effect into account, we used a speciation model for Fe(II)-oxidation kinetics developed by King (1998). This model uses a Pitzer ion interaction framework to calculate the ion activity coefficients of different Fe(II) species in carbonated seawater. Rate constants for individual Fe(II) species are derived from best fits to available rate measurements in carbonated media at low and high ionic strength.

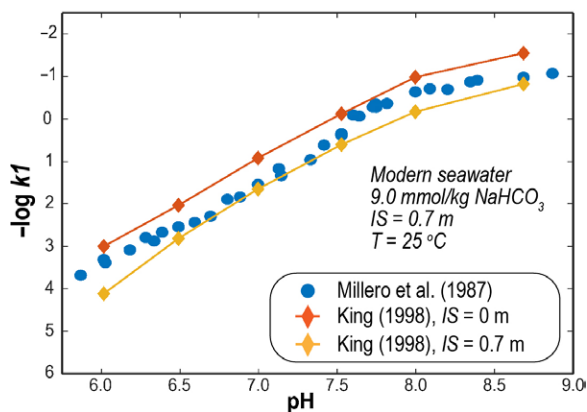


Figure 3. Comparison of modeled (King, 1998) and measured (Millero et al., 1987) rates of Fe(II) oxidation in artificially carbonated modern seawater using thermodynamic parameters from King (1998). k —rate constant for Fe(II) oxidation by $O_2(aq)$; IS —ionic strength (mol/kg); T —temperature ($^{\circ}C$). Results show that estimated and measured rates of Fe(II) oxidation are in close agreement.

Overall Fe(II)-oxidation rates are calculated as a weighted average of individual oxidation rates of Fe(II)-aqueous species. Model calculations show that at $SiO_2(aq)$ concentrations at amorphous silica solubility and $\log pCO_2 = -2.0$ (Blättler et al., 2016), Fe(II)-carbonate species begin to dominate above pH 7 (Fig. DR3). The overall Fe(II)-oxidation rates predicted by the model are in excellent agreement with laboratory measurements (Fig. 3).

Greenalite Precipitation and Fe^{2+} -Oxidation Rates

In order to constrain oxygen concentrations during deposition, we used our kinetic model to compare rates of greenalite precipitation and Fe^{2+} oxidation as a function of pH and atmospheric O_2 content at three different total Fe concentrations (i.e., 10, 100, and 1000 $\mu mol/kg$ Fe^{2+}). All three examples showed that under large ranges in pH and Fe(II) concentration, low $O_2(aq)$ is required for greenalite precipitation to outpace Fe(II) oxidation (Fig. 4; Figs. DR4–DR6), and therefore generation and preservation of greenalite-rich sediments. For example, at a total Fe(II) concentration of 100 $\mu mol/kg$, a pO_2 of $10^{-6} \times PAL$ would allow more rapid greenalite precipitation than Fe(II) oxidation only at high pH (>7.75) (Fig. 4). In contrast, a pO_2 of $10^{-7} \times PAL$ would allow greenalite to form with little to no Fe oxidation over a larger pH range (pH ≥ 7.1). Using recent estimates for ocean pH during deposition of the Griquatown BIFs (pH ~ 7 ; Halevy and Bachan, 2017), our model predicts that oxygen concentrations must have been $<10^{-7} \times PAL$ for rates of greenalite precipitation to exceed Fe^{2+} oxidation assuming Fe^{2+} concentrations of 100 $\mu mol/kg$.

IMPLICATIONS OF GREENALITE PRECIPITATION IN SHALLOW OCEANS

Our observations from the Griquatown Iron Formation imply that Fe oxidation, whether biotic or abiotic, did not control iron deposition. The precipitation of greenalite in well-mixed, shallow seawater provides important constraints

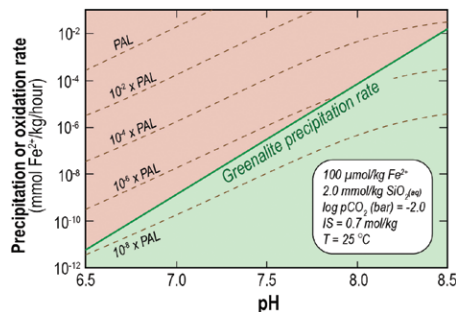


Figure 4. Greenalite precipitation versus Fe(II) oxidation rates as function of pO_2 and pH for 100 $\mu mol/kg$ Fe^{2+} . Brown curves below green line (shaded light green) represent pO_2 values at which rate of greenalite precipitation exceeds that of Fe(II) oxidation. Red shading above green line represents areas where Fe(II) oxidation exceeds greenalite precipitation. PAL—present atmospheric levels; IS—ionic strength (mol/kg); T—temperature ($^{\circ}C$).

on the oxygen content of the surface ocean at continental margins. Our estimates imply that the shelf on which the Griquatown Iron Formation was deposited was devoid of oxygen ($<10^{-6} \times PAL$) at ca. 2.45 Ga. These estimates are consistent with rare-earth-element data (Planavsky et al., 2010) and iodine data (Hardisty et al., 2014), which indicate that late Archean shallow-water environments were essentially anoxic, but contradicts interpretations based on trace-element data for free oxygen in the surface ocean before the GOE.

The presence of anoxic shallow oceans at ca. 2.45 Ga is consistent with a relatively late evolution of the oxygenic Cyanobacteria (Soo et al., 2017; Betts et al., 2018) based on recent molecular clock estimates, and with arguments that redox buffers would have been overwhelmed by newly produced oxygen within 0.1 m.y. of the emergence of oxygenic photosynthesis (Ward et al., 2016). Although our results do not preclude the possibility that oxygenic photosynthesis evolved long before the GOE, they favor the view that it appeared after 2.45 Ga, and was the principal driver of atmospheric oxygenation.

ACKNOWLEDGMENTS

Rasmussen acknowledges support from the Australian Research Council (ARC grants DP140100512 and DP190102237) and Geological Processes and Mineral Resources (GPMR) Open Research Grant GPMR201802. Support for Tosca was provided by the Natural Environment Research Council (NERC grant NE/M013014/1) and the Leverhulme Trust. Tsikos thanks Assmang Ltd. (South Africa) for support and South32 (Perth, Australia) for access to drill core. SEM, FIB, and TEM analyses were performed at the Centre for Microscopy, Characterization and Analysis at the University of Western Australia, a node of Microscopy Australia funded from university and government sources. The manuscript benefitted from comments by three anonymous referees.

REFERENCES CITED

- Bennett, R.H., Bryant, W.R., and Keller, G.H., 1981, Clay fabric of selected submarine sediments: Fundamental properties and models: *Journal of Sedimentary Petrology*, v. 51, p. 217–232, <https://doi.org/10.1306/2127FC52-2B24-11D7-8648000102C1865D>.
- Betts, H.C., Puttick, M.N., Clark, J.W., Williams, T.A., Donoghue, P.C.J., and Pisani, D., 2018, Integrated genomic and fossil evidence illuminates life's early evolution and eukaryote origin: *Nature Ecology and Evolution*, v. 2, p. 1556–1562, <https://doi.org/10.1038/s41559-018-0644-x>.
- Beukes, N.J., 1984, Sedimentology of the Kuruman and Griquatown Iron-formations, Transvaal Supergroup, Griqualand West, South Africa: *Precambrian Research*, v. 24, p. 47–84, [https://doi.org/10.1016/0301-9268\(84\)90069-X](https://doi.org/10.1016/0301-9268(84)90069-X).
- Beukes, N.J., and Gutzmer, J., 2008, Origin and paleoenvironmental significance of major iron formations at the Archean-Paleoproterozoic boundary: *Reviews in Economic Geology*, v. 15, p. 5–47.
- Blättler, C.L., Kump, L.R., Fischer, W.W., Paris, G., Kasbohm, J.J., and Higgins, J.A., 2016, Constraints on ocean carbonate chemistry and pCO_2 in the Archean and Palaeoproterozoic: *Nature Geoscience*, v. 10, p. 41–45, <https://doi.org/10.1038/ngeo2844>.
- Czaja, A.D., Johnson, C.M., Roden, E.E., Beard, B.L., Voegelin, A.R., Nägler, T.F., Beukes, N.J., and Wille, M., 2012, Evidence for free oxygen in the Neoproterozoic ocean based on coupled iron-molybdenum isotope fractionation: *Geochimica et Cosmochimica Acta*, v. 86, p. 118–137, <https://doi.org/10.1016/j.gca.2012.03.007>.
- Deirich, A., Chang, I.Y., Whittaker, M.L., Weigand, S., Keane, D., Rix, J., Germaine, J.T., Joester, D., and Flemings, P.B., 2018, Particle arrangements in clay slurries: The case against the honeycomb structure: *Applied Clay Science*, v. 152, p. 166–172, <https://doi.org/10.1016/j.clay.2017.11.010>.
- Fischer, W.W., and Knoll, A.H., 2009, An iron shuttle for deepwater silica in Late Archean and early Paleoproterozoic iron formation: *Geological Society of America Bulletin*, v. 121, p. 222–235, <https://doi.org/10.1130/B26328.1>.
- Fischer, W.W., Hemp, J., and Johnson, J.E., 2016, Evolution of oxygenic photosynthesis: *Annual Review of Earth and Planetary Sciences*, v. 44, p. 647–683, <https://doi.org/10.1146/annurev-earth-060313-054810>.
- Guggenheim, S., Bailey, S.W., Eggleton, R.A., and Wilkes, P., 1982, Structural aspects of greenalite and related minerals: *Canadian Mineralogist*, v. 20, p. 1–18.
- Halevy, I., and Bachan, A., 2017, The geologic history of seawater pH: *Science*, v. 355, p. 1069–1071, <https://doi.org/10.1126/science.aal4151>.

- Hardisty, D.S., Lu, Z., Planavsky, N.J., Bekker, A., Philippot, P., Zhou, X., and Lyons, T.W., 2014, An iodine record of Paleoproterozoic surface ocean oxygenation: *Geology*, v. 42, p. 619–622, <https://doi.org/10.1130/G35439.1>.
- Johnson, J.E., Muhling, J.R., Cosmidis, J., Rasmussen, B., and Templeton, A.S., 2018, Low-Fe(III) greenalite was a primary mineral from Neoproterozoic oceans: *Geophysical Research Letters*, v. 45, p. 3182–3192, <https://doi.org/10.1002/2017GL076311>.
- Kase, Y., Sato, M., Nishida, N., Ito, M., Mukti, M.M., Ikehara, K., and Takizawa, S., 2016, The use of microstructures for discriminating turbiditic and hemipelagic muds and mudstones: *Sedimentology*, v. 63, p. 2066–2086, <https://doi.org/10.1111/sed.12296>.
- King, D.W., 1998, Role of carbonate speciation on the oxidation rate of Fe(II) in aquatic systems: *Environmental Science & Technology*, v. 32, p. 2997–3003, <https://doi.org/10.1021/es980206o>.
- Konhauser, K.O., Amskold, L., Lalonde, S.V., Posth, N.R., Kappler, A., and Anbar, A., 2007, Decoupling photochemical Fe(II) oxidation from shallow-water BIF deposition: *Earth and Planetary Science Letters*, v. 258, p. 87–100, <https://doi.org/10.1016/j.epsl.2007.03.026>.
- Konhauser, K.O., et al., 2017, Iron formations: A global record of Neoproterozoic to Palaeoproterozoic environmental history: *Earth-Science Reviews*, v. 172, p. 140–177, <https://doi.org/10.1016/j.earscirev.2017.06.012>.
- Kump, L.R., and Barley, M.E., 2007, Increased subaerial volcanism and the rise of atmospheric oxygen 2.5 billion years ago: *Nature*, v. 448, p. 1033–1036, <https://doi.org/10.1038/nature06058>.
- Lasaga, A.C., 1998, *Kinetic Theory in the Earth Sciences*: Princeton, New Jersey, Princeton University Press, 811 p., <https://doi.org/10.1515/9781400864874>.
- Luo, G., Ono, S., Beukes, N.J., Wang, D.T., Xie, S., and Summons, R.E., 2016, Rapid oxygenation of Earth's atmosphere 2.33 billion years ago: *Science Advances*, v. 2, e1600134, <https://doi.org/10.1126/sciadv.1600134>.
- Millero, F.J., Sotolongo, S., and Izaguirre, M., 1987, The oxidation kinetics of Fe(II) in seawater: *Geochimica et Cosmochimica Acta*, v. 51, p. 793–801, [https://doi.org/10.1016/0016-7037\(87\)90093-7](https://doi.org/10.1016/0016-7037(87)90093-7).
- Pavlov, A.A., and Kasting, J.F., 2002, Mass-independent fractionation of sulfur isotopes in Archean sediments: Strong evidence for an anoxic Archean atmosphere: *Astrobiology*, v. 2, p. 27–41, <https://doi.org/10.1089/153110702753621321>.
- Planavsky, N., Bekker, A., Rouxel, O.J., Kamber, B., Hofmann, A., Knudsen, A., and Lyons, T.W., 2010, Rare earth element and yttrium compositions of Archean and Paleoproterozoic iron formations revisited: New perspectives on the significance and mechanisms of deposition: *Geochimica et Cosmochimica Acta*, v. 74, p. 6387–6405, <https://doi.org/10.1016/j.gca.2010.07.021>.
- Rasmussen, B., Krapež, B., and Muhling, J.R., 2015a, Seafloor silicification and hardground development during deposition of 2.5 Ga banded iron formations: *Geology*, v. 43, p. 235–238, <https://doi.org/10.1130/G36363.1>.
- Rasmussen, B., Krapež, B., Muhling, J.R., and Suvorova, A., 2015b, Precipitation of iron silicate nanoparticles in early Precambrian oceans marks Earth's first iron age: *Geology*, v. 43, p. 303–306, <https://doi.org/10.1130/G36309.1>.
- Rasmussen, B., Muhling, J.R., Suvorova, A., and Krapež, B., 2017, Greenalite precipitation linked to the deposition of banded iron formations downslope from a late Archean carbonate platform: *Precambrian Research*, v. 290, p. 49–62, <https://doi.org/10.1016/j.precamres.2016.12.005>.
- Rasmussen, B., Muhling, J.R., and Fischer, W.W., 2019, Evidence from laminated chert in banded iron formations for deposition by gravitational settling of iron-silicate muds: *Geology*, v. 47, p. 167–170, <https://doi.org/10.1130/G45560.1>.
- Satkoski, A.M., Beukes, N.J., Li, W., Beard, B.L., and Johnson, C.M., 2015, A redox-stratified ocean 3.2 billion years ago: *Earth and Planetary Science Letters*, v. 430, p. 43–53, <https://doi.org/10.1016/j.epsl.2015.08.007> (corrigendum available at <https://doi.org/10.1016/j.epsl.2016.12.013>).
- Shih, P.M., Hemp, J., Ward, L.M., Matzke, N.J., and Fischer, W.W., 2017, Crown group Oxyphotobacteria postdate the rise of oxygen: *Geobiology*, v. 15, p. 19–29, <https://doi.org/10.1111/gbi.12200>.
- Soo, R.M., Hemp, J., Parks, D.H., Fischer, W.W., and Hugenholtz, P., 2017, On the origins of oxygenic photosynthesis and aerobic respiration in Cyanobacteria: *Science*, v. 355, p. 1436–1440, <https://doi.org/10.1126/science.aal3794>.
- Tosca, N.J., Guggenheim, S., and Pufahl, P.K., 2016, An authigenic origin for Precambrian greenalite: Implications for iron formation and the chemistry of ancient seawater: *Geological Society of America Bulletin*, v. 128, p. 511–530, <https://doi.org/10.1130/B31339.1>.
- Ward, L.M., Kirschvink, J.L., and Fischer, W.W., 2016, Timescales of oxygenation following the evolution of oxygenic photosynthesis: *Origins of Life and Evolution of the Biosphere*, v. 46, p. 51–65, <https://doi.org/10.1007/s11084-015-9460-3>.
- Zahnle, K.J., Claire, M., and Catling, D., 2006, The loss of mass-independent fractionation in sulfur due to a Paleoproterozoic collapse of atmospheric methane: *Geobiology*, v. 4, p. 271–283, <https://doi.org/10.1111/j.1472-4669.2006.00085.x>.

Printed in USA